

Spectroscopy of diagnostically-important magnetic-dipole lines in highly-charged $3d^n$ ions of tungsten

Yu. Ralchenko,^{*} I.N. Draganić,[†] D. Osin, J.D. Gillaspy, and J. Reader

National Institute of Standards and Technology,

Gaithersburg, Maryland 20899-8422

(Dated: October 8, 2018)

Abstract

An electron beam ion trap (EBIT) is used to measure extreme ultraviolet spectra between 10 nm and 25 nm from highly-charged ions of tungsten with an open $3d$ shell (W XLVIII through W LVI). We found that almost all strong lines are due to the forbidden magnetic-dipole (M1) transitions within $3d^n$ ground configurations. A total of 37 spectral lines are identified for the first time using detailed collisional-radiative (CR) modeling of the EBIT spectra. A new level-merging scheme for compactification of rate equations is described. The CR simulations for Maxwellian plasmas show that several line ratios involving these M1 lines can be used to reliably diagnose temperature and density in hot fusion devices.

^{*} Electronic mail: yuri.ralchenko@nist.gov

[†] Current address: Oak Ridge National Laboratory, Oak Ridge TN 37831-6372

I. INTRODUCTION

Spectroscopy of highly-charged ions of high-Z elements is currently the subject of extensive research. From a theoretical viewpoint, the accurately measured wavelengths, energy levels and transition probabilities provide crucial tests for advanced theories of atomic structure in a regime where relativistic and quantum-electrodynamic effects become very strong. As for applications, since tungsten is currently considered to be a primary candidate for the plasma-facing material in the ITER divertor region [1], the spectra of its ions in a wide range of wavelengths are being studied under various conditions. It is not surprising, therefore, that a large number of research papers on the spectra of tungsten ions measured with electron beam ion traps (EBIT) [2–13], tokamaks [14–16], stellarators [17] and other high-temperature-plasma devices were published over the last decade. A detailed compilation of the recent results on spectral lines and spectra of W can be found in Refs. [18, 19].

In the ITER plasma, the tungsten ions will be transported from the relatively cold divertor region to the plasma core with temperatures on the order of 20 keV. Although considerable efforts are to be spent to minimize radiative power losses due to emission from highly-charged ions of W, very useful information for plasma diagnostics can be derived from isolated spectral lines. For instance, the electron temperature T_e can be easily found from the ratios of strong lines from different ions through the dependence of the ionization balance on T_e , and the ion temperature can be derived from the line shapes. Determination of the electron density n_e from spectral lines, however, is not as straightforward. Most often it involves a comparison of allowed and forbidden lines, and thus this technique relies upon knowledge of wavelengths and transition probabilities of the involved spectral lines. At high densities, when level populations approach the local thermodynamic equilibrium (LTE), or Boltzmann, limit, forbidden lines with transition probabilities many orders of magnitude smaller than those for allowed electric-dipole (E1) transitions are too weak to be observed in the spectrum. In low density plasmas, however, the populations of the excited levels which decay only via forbidden transitions can be relatively high and therefore result in strong intensities. For each forbidden line there exists a transition range of electron densities where electron collisions are comparable to the radiative decay rate. It is in this range of densities that one may hope to use a particular forbidden line for density diagnostics.

Currently, more than 80 forbidden lines in tungsten ions, from W^{28+} to W^{57+} , are known

from experimental measurements [20]. The high-multipole lines from W ions were observed, for instance, in x-rays [7, 12, 21–23], extreme ultraviolet (EUV) [9, 10, 14], vacuum ultraviolet [24] and ultraviolet (UV) [2, 3] ranges of spectra in tokamaks and EBITs. The probabilities of forbidden transitions show very strong increase with the ion charge while the collisional damping of spectral lines becomes less effective due to a decrease of cross sections. As a result, the forbidden lines are more prominent in the spectra of multiply-charged ions.

Forbidden transitions in highly-charged ions are also a subject of active theoretical research with emphasis on their use in plasma diagnostics. The visible/UV magnetic-dipole (M1) $J = 2 - 3$ line in Ti-like ions was analyzed for density diagnostics in hot plasmas since the pioneering work of Feldman et al. [25]. Continuing this work, Feldman et al. [26, 27] performed a systematic study of density-sensitive M1 lines in Ti-like ions and in various N-shell ions. Recently Jonauskas et al. [28] calculated wavelengths and transition probabilities of M1 lines in $4d^n$ configurations of W ions using large-scale configuration-interaction methods. Also, Quinet et al. [29] performed Hartree-Fock calculations of allowed and forbidden transitions in W I–III, addressing in particular the diagnostics of fusion plasmas. An extensive calculation of atomic characteristics of eight isoelectronic sequences of tungsten ions in a broad range of wavelengths and transitions was recently performed by Safronova and Safronova using the relativistic many-body perturbation theory (RMBPT) [30]. The number of theoretical works on spectral lines and transition probabilities in ions of tungsten is too large to cite here, so we refer the reader to the bibliographic databases at the National Institute of Standards and Technology (NIST) for an extensive list of publications on tungsten [31].

An example of a density-sensitive line ratio in highly-charged tungsten ions can be provided by the ratio of electric-quadrupole (E2) and magnetic-octupole (M3) lines in Ni-like W^{46+} [32]. These two close lines at about 0.793 nm are due to two $3d^{10}-3d^94s$ parity-conserving transitions. They were experimentally resolved only recently [12], although the unresolved spectral feature was known for several years from tokamak [21] and EBIT [7] measurements. A large difference in transition probabilities for these lines, on the order of 10^6 , results in a different response to collisional destruction of level populations. As was shown in Ref. [32], the E2/M3 line ratio in W^{46+} can be used for density diagnostics in the range of typical values of n_e in tokamaks.

The goal of the present work is to study the magnetic-dipole transitions within the ground

configurations of the $3d^n$ ions of tungsten using the NIST EBIT. Previously we reported several EUV lines in Co-, Ca- and K-like ions [8, 9] within configurations $3d^9$, $3d^2$ and $3d$, respectively. Here we extend our measurements to include the remaining ions of tungsten with open $3d$ shell. Using detailed collisional-radiative (CR) modeling, we identify the measured spectral lines in the EUV range of spectra between 10 nm and 25 nm. In addition, we perform CR simulations to explore potential use of the newly identified lines for diagnostics of hot fusion plasmas.

The paper is organized as follows. Section II describes the experiment and measurement of the spectra. Details of the CR modeling are presented in Section III. We then discuss the identification of the new M1 lines. Section V presents the analysis of the line ratios that can be used for density diagnostics in fusion plasmas. Finally, the last Section summarizes our conclusions.

II. EXPERIMENT

The measurements of spectra from the $3d^n$ ions of tungsten were performed at the NIST EBIT facility [33] using a grazing-incidence EUV spectrometer [34]. The photons were collected by a spherical gold-coated mirror. A 1:1 image of the EBIT plasma column was focused onto the spectrometer entrance slit. The mirror center was at an equal distance of 480 mm from the EBIT axis and the spectrometer entrance slits. The photons were dispersed with a reflection flat-field grating with 1200 lines/mm. The grazing incidence angle for both the mirror and the grating was 3° . The slit width was kept at $500 \mu\text{m}$ resulting a constant resolving power of about 350. The EUV spectra were directly recorded by a liquid nitrogen cooled back-illuminated charge-coupled device (CCD) that was placed in the focal plane of the grating at a distance of 235 mm. The CCD detector has an array of 1340×400 pixels ($20 \mu\text{m} \times 20 \mu\text{m}$ each). A detailed description of our EUV spectroscopic system can be found in [34].

The spectra were measured in two separate runs, one in 2008 (run A) and another in 2010 (run B). The nominal electron beam energies in run A were 4500 eV, 4750 eV, 5000 eV, 5250 eV, 5500 eV, 6000 eV, and 7000 eV, and the observed spectra were in the range between 4.5 nm and 19.5 nm. A theoretical analysis of the spectra indicated that some additional lines may have longer wavelengths and therefore the second run of measurements

was initiated. The beam energies for run B were selected to be complementary to those for run A, namely, 4665 eV, 4840 eV, 5155 eV, 5355 eV, 5755 eV, and 6500 eV, and the observed spectral window was shifted to 8 nm to 26 nm by translating the detector in the focal plane. The electron beam current for both runs was 150 mA and the trap depth was approximately 220 V. The trap was emptied and reloaded every 11 s.

The measured spectra of tungsten were calibrated with lines from lighter elements. Reference spectra of Ne, Ar, O, and Fe were measured at several energies between 2 keV and 9 keV for run A. The calibration of spectra for run B was performed with lines from N, O, Fe and Kr at beam energies between 1 keV and 16 keV. Both gas injection [35] and metal vapour vacuum arc ion source (MEVVA) [36] systems were utilized in the calibration runs. The observed calibration lines were fitted with the statistically-weighted Gaussian line profiles. The calibration curve was a fourth-order polynomial fit of the line centers (CCD pixel number) to the known wavelengths. The weighting in the fit to the calibration curve was based on the quadrature sum of the statistical uncertainty of our observation of the calibration line center, the accuracy of the calibration line wavelength, and estimated systematic measurement uncertainty. When a wavelength was measured at various beam energies, the final wavelength was taken to be the weighted average of the corresponding values (with exceptions noted below), while the total error in the final wavelength was taken to be the quadrature sum of the total uncertainty from the calibration curve and the reduced statistical uncertainty from the average at various energies. The statistical uncertainties in the line positions were typically less than 0.001 nm. The final accuracy of the W spectral lines was 0.003 nm.

The measured spectra for tungsten are shown in Figs. 1 (beam energies $E_B = 4500$ eV to 5250 eV) and 2 (beam energies $E_B = 5355$ eV to 7000 eV). The run-A spectra are shown in black and the run-B spectra are presented in red (color online only). The spectral region in the figures is limited to $\lambda = 10$ nm to 20 nm since almost all M1 lines from the $3d^n$ ions are within this range. Only one line, $\lambda \approx 21.203$ nm in the V-like ion, was found above 20 nm, and therefore we do not show the run B spectra at longer wavelengths. The identified transitions in various ions of tungsten are indicated by vertical dashed lines in the plots. The measured spectra also contain a few impurity lines from oxygen (e.g., at 15 nm) and xenon, which are marked by asterisks. The highest-energy spectrum of $E_B = 7000$ eV also shows a few lines from Ar- and Cl-like ions which have already been identified in our previous work

[9].

III. COLLISIONAL-RADIATIVE MODELING OF EBIT SPECTRA

Generally, identification of measured spectral lines greatly benefits from applying methods that include comparisons of different physical parameters, such as wavelengths and intensities. While atomic structure methods for simple ions can calculate wavelengths with the accuracy at the level of 0.01% or even better, the simulations for multi-electron ions with open shells may not be as precise as needed for unambiguous line identification. Another often used technique in EBIT studies is the analysis of the variation of line intensity with beam energy. This method, however, would only be of marginal value when neighboring ions do not differ much in ionization energy, and therefore it is difficult to uniquely associate a line with a specific ionization stage.

The most reliable analysis of spectral lines can be accomplished with a collisional-radiative modeling of EBIT plasmas. For any given set of plasma parameters, such as beam energy and density, the CR simulations can produce a detailed synthetic spectrum containing lines from a number of ions. A comparison of calculated line positions and line intensities with the spectra measured at several energies provides practically unambiguous identification of spectral lines. This method was successfully used in our previous publications [7–11] in order to analyze and identify dozens of spectral lines from highly-charged heavy ions in x-ray and EUV regions.

In this work we implement the non-Maxwellian collisional-radiative code NOMAD [37] for the calculation of spectra from tungsten ions in the EBIT. The solution of the steady-state rate equation

$$\hat{A} \cdot \hat{N} = 0 \tag{1}$$

provides populations of all relevant atomic states and, consequently, intensities of spectral lines. Here \hat{N} is the vector of populations of atomic states included in simulations and \hat{A} is the rate matrix describing physical processes that affect state populations. The detailed representation of Eq. (1) is:

$$\sum_{j>i} N_{z,j} \cdot \left(A_{z,ij}^{rad} + n_e R_{z,ij}^{dx} \right) + \sum_{j<i} N_{z,j} n_e R_{z,ij}^{ex} + \sum_k n_e R_{z-1,ki}^{ion} + \sum_k n_e R_{z+1,ki}^{rr} + \delta_{i1} n_0 R_{z+1}^{cx}$$

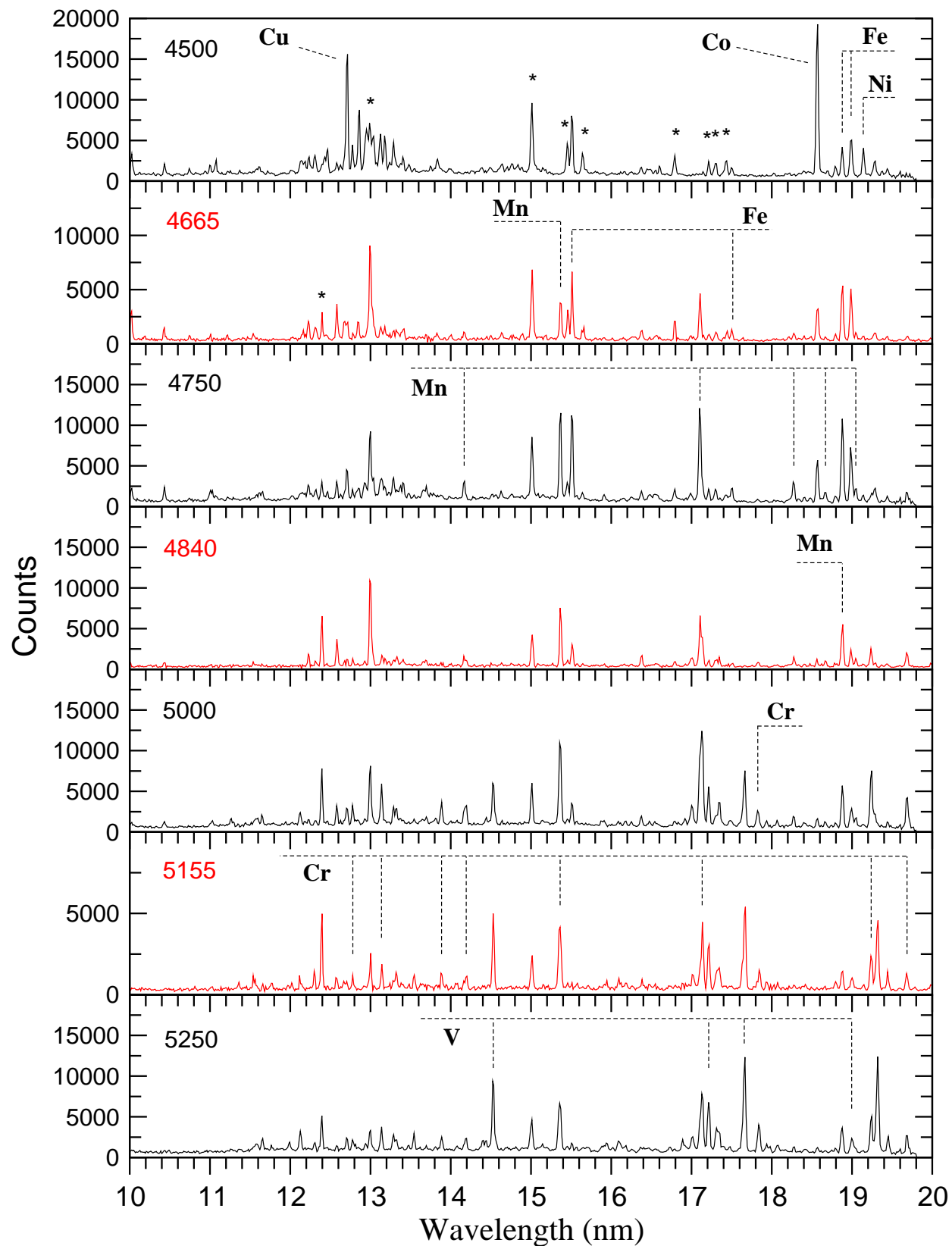


FIG. 1. Tungsten spectra between 10 nm and 20 nm for beam energies between 4500 eV and 5250 eV. The identified transitions are indicated by vertical dashed lines. The spectra from run A are shown in black and the spectra from run B are shown in red. Asterisks show the strongest impurity lines.

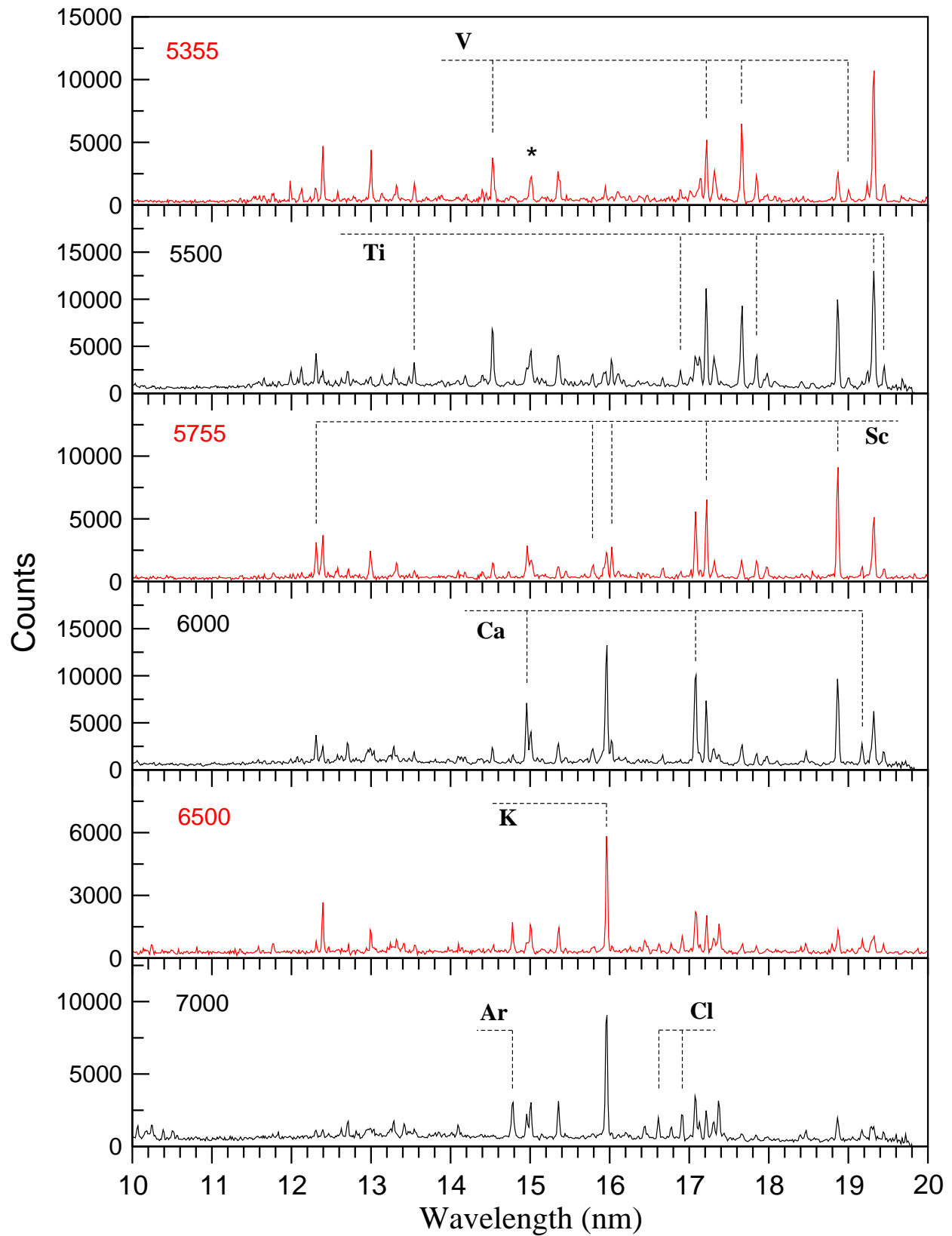


FIG. 2. Tungsten spectra between 10 nm and 20 nm for beam energies between 5355 eV and 7000 eV. The identified transitions are indicated by vertical dashed lines. The spectra from run A are shown in black and the spectra from run B are shown in red. Asterisks show the strongest impurity lines.

$$-N_{z,i} \left(\sum_{j<i} (A_{z,ji}^{rad} + n_e R_{z,ji}^{dx}) + \sum_{j>i} n_e R_{z,ji}^{ex} + \sum_k n_e R_{z,ki}^{ion} + \sum_m n_e R_{z,mi}^{rr} + \delta_{i1} n_0 R_z^{cx} \right) = 0 \quad (2)$$

where $N_{z,i}$ is the population of atomic state j in an ion z , $A_{z,ij}^{rad}$ is the radiative transition probability, n_e is the electron density, $R_{z,ij}^{ex}$, $R_{z,ij}^{dx}$, and $R_{z-1,ki}^{ion}$ are the rate coefficients for electron-impact excitation, deexcitation and ionization, respectively, $R_{z,mi}^{rr}$ is the rate coefficient for radiative recombination, n_0 is the density of the neutrals in the trap, and R_z^{cx} is the rate coefficient for the charge exchange (CX) between neutrals and W ions. Unlike Maxwellian plasmas, dielectronic capture (DC) is normally neglected in EBIT collisional-radiative simulations since this resonant process requires an accurate match of the beam energy with the DC energy.

Charge exchange between the W ions and neutrals in the ion trap can affect the ionization distribution. The Kronecker factor δ_{i1} in Eq. (2) indicates that in our model the CX connects only the ground states of adjacent ions. It is worth noting that since the ion charge is so high ($z \approx 50$), the contribution of double CX may be comparable to the single CX. We are unaware of any calculations or measurements of single or multiple CX cross sections between highly-charged tungsten and neutral atoms or molecules, and therefore the Classical Trajectory Monte Carlo cross section scaling [38]

$$\sigma_{cx} = z \cdot 10^{-15} \text{ cm}^2 \quad (3)$$

was used in calculations. In fact, the precise value of this parameter is not very important as it enters the rate equations as a factor in the product $n_0 v_0 \sigma_{cx}$, where v_0 is the relative velocity between neutrals and tungsten ions. Neither n_0 nor v_0 are accurately known for our experimental conditions, so that the product $n_0 v_0$ was used as the only free parameter in CR simulations.

The NOMAD code solves the rate equations (1) using externally calculated basic atomic data. For the present work the energy levels, radiative transition probabilities (up to electric and magnetic octupoles) and electron-impact collisional cross sections were calculated with the relativistic Flexible Atomic Code (FAC), which is described in detail in Ref. [39]. The relativistic atomic structure (including quantum-electrodynamics corrections) and collision methods implemented in FAC are well suited for highly-charged ions of heavy elements. Our CR model contains 15 ions, from Zn-like W^{44+} to Si-like W^{60+} . Since the ions with ionization potentials I_z larger than the beam energy E_b have very small populations, only

6 to 8 ionization stages were kept for each specific simulation. The atomic states for each ion contained single and double ($\Delta n = 0$ only) excitations from the ground configuration. Single excitations from the $3l$ subshells were included up to $n = 5$ for most of the open-shell ions, and up to $n = 7$ or 8 for closed-shell (Ni-like) ions or ions with one or two electrons above closed shells. The double excitations are included only for $\Delta n = 0$ within $n=3$ shell.

In our previous works on high- Z ions with open s and p shells [7–11] all singly- and doubly-excited states included in the CR modeling were atomic *levels*, i.e., the fine-structure components. Since open $3d^n$ shells allow many more permitted combinations of angular momenta, the total number of atomic levels due to single and double excitations from $3s^23p^63d^n$ increases drastically and becomes untractable with available computational facilities. While a typical number of levels in CR modeling of $4s^24p^n$ and $3s^23p^n$ ions was on the order of 1000 per ionization stage, the excitations from $3s^23p^63d^n$ can generate 10,000 levels or more, and thus the total number of levels becomes prohibitively large.

In order to reduce the size of the rate equations to an acceptable level, the atomic states within each $3d^n$ ion were divided into two groups. The first group was composed of the ground configuration levels $3s^23p^63d^n$ and singly- and doubly-excited levels within the same $n=3$ shell, i.e., $3s^23p^53d^{n+1}$, $3s3p^63d^{n+1}$, $3s^23p^43d^{n+2}$, $3s3p^53d^{n+2}$, and $3p^63d^{n+2}$. The levels in this first group were retained without modification as the fine-structure components. The levels in the second group, i.e., $\Delta n \geq 1$ excitations $3s^23p^63d^{n-1}kl$, $3s^23p^53d^nkl$ and $3s3p^63d^nkl$ with $k \geq 4$, were joined into generalized atomic states, which are referred to as the “superterms” below. The procedure of level grouping can be exemplified for the $3d^{n-1}kl$ configuration. Each of the atomic levels within this configuration can be described by the following set of quantum numbers in jj-coupling (FAC level notations are given in this coupling scheme): $((3d_-^a)_{j_-}, (3d_+^b)_{j_+})_{j_c}, (kl)_{j_k})_J$ or simply $((j_-, j_+)_{j_c}, j_k)_J$ where $a+b = n-1$, j_- and j_+ are the momenta of the $3d_-$ and $3d_+$ sub-shells, j_c is the total angular momentum of the core $3d^{n-1}$, $j_k = l \pm 1/2$ is the momentum of the optical electron kl , and J is the total angular momentum. Here and below we use notation l_{\pm} for an l electron with $j = l \pm 1/2$. The simplest procedure in level grouping would be to join them according to the atomic jj-terms $((j_-, j_+)_{j_c}, j_k)$. However, the reduction in the total number of states is rather small. Even the next level of grouping, based on the core momentum j_c , results in several thousands of states per ion. Therefore the excited levels in the present work were joined according to the (j_-, j_+) pairs. For the high excited configurations with a hole in the $3s$ or $3p$ subshell, the

levels were combined by the three momenta (j_h, j_-, j_+) where j_h is the hole momentum. We found that while such grouping significantly reduces the total number of states per ion, the resulting set of superterms provides a sufficiently dense representation of atomic structure for each of the $3d^n$ ions in our CR model. The actual reduction in the number of states in an ion can reach an order of magnitude: for instance, for the V-like ion with $3d^5$ ground configuration the originally generated 10801 levels are reduced to 791 fine-structure levels and 465 superterms only. This method of including lowest atomic levels and highly-excited generalized states is similar to the recently proposed hybrid CR models [40] for high-density plasma kinetics, where the highly-excited levels are combined into even more general groups of states, namely, configurations or superconfigurations.

Another feature of our calculations is the additional correction of calculated energies for the $3d^n$ levels. For each of these ions we performed another calculation with the FAC code including, in addition to configurations mentioned above, all possible excitations within the $n=3$ complex. (Obviously, the total complex was already included for $3d^9$ and $3d^8$ ions.) The energies of the ground state configurations in the CR model were then replaced by the newly calculated energies which, although different by a fraction of a percent only, still improved the agreement with the experimental energies and wavelengths. A similar procedure was applied in our recent work on EUV spectra from highly-charged ions of Hf, Ta and Au [41].

The transition probabilities and cross sections between the levels and the superterms or between the superterms were derived from the FAC results for transitions between atomic levels using statistical averaging. The collisional cross sections were then convolved with a 45-eV-wide Gaussian electron-energy distribution function of the EBIT beam in order to generate the rate coefficients. The final set of rate equations (1) was solved in the steady-state approximation for a grid of beam energies between 4300 eV and 7000 eV. For each energy the charge-exchange parameter n_0v_0 varied between 10^{13} and $3 \cdot 10^{14} \text{ cm}^{-2}\text{s}^{-1}$. The ionization distributions, level populations, and spectral line intensities were calculated for each combination of E_b and n_0v_0 , and the spectral patterns were compared with the measured spectra to find the best agreement. The best value of n_0v_0 was found to be about $10^{14} \text{ cm}^{-2}\text{s}^{-1}$. This agrees with our order-of-magnitude estimates of 10^7 cm^{-3} for the density of neutrals and 10^7 cm/s for the relative velocity.

An example of comparison between the experimental and calculated spectra is presented in Fig. 3. The simulated spectrum for the beam energy of 5150 eV with $n_0v_0 = 10^{14} \text{ cm}^{-2}\text{s}^{-1}$

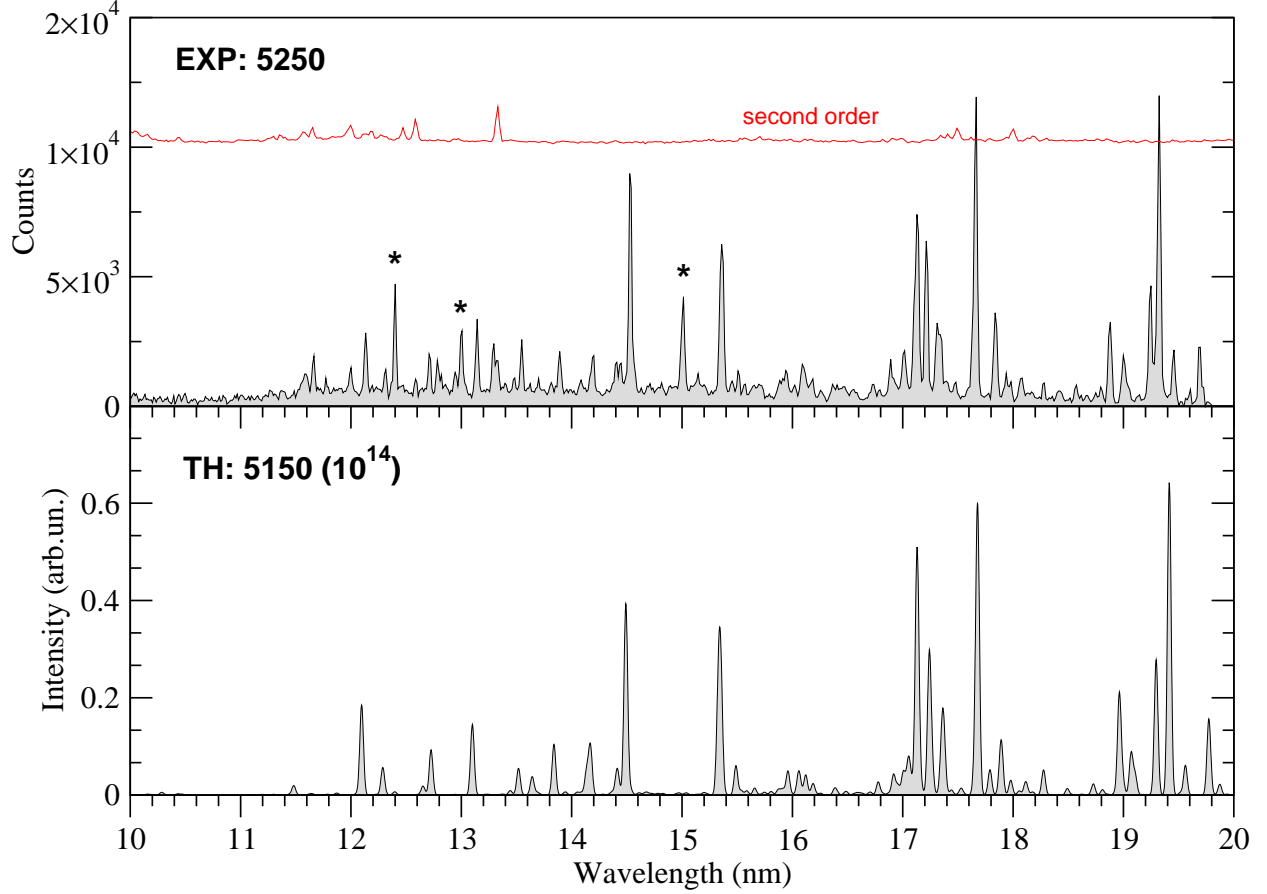


FIG. 3. Comparison of experimental spectrum at the nominal beam energy of 5250 eV (top) and calculated spectrum at 5150 eV and $n_0 v_0 = 10^{14} \text{ cm}^{-2} \text{ s}^{-1}$. The second order spectrum is shown by the shifted line and the strongest impurity lines from Xe (12.4 nm and 13.0 nm) and O (15.0 nm) are indicated by asterisks.

and CX cross section from Eq. (3) (bottom) agrees very well with the measured spectral pattern at the nominal beam energy of 5250 eV (top); this energy difference is attributed to the space charge effects in the trap. The three strong lines at 12.4 nm, 13.0 nm, and 15.0 nm marked by asterisks are due to xenon and oxygen impurities. Also, Fig. 3 (top) shows the second order spectrum shifted along the vertical axis in order to indicate a few relatively weak second-order lines. One can see that both line positions and line intensities are reproduced in our simulations very accurately so that most of the lines can be identified from the visual comparison. Such a good agreement was observed for all cases considered in the present work.

IV. LINE IDENTIFICATION

Table I presents the strongest identified lines between 10 nm and 25 nm in the experimental spectra of runs A and B. Almost all lines in this table are the forbidden magnetic-dipole transitions within the ground configurations $3d^n$ of tungsten ions from Co-like W^{47+} to K-like W^{55+} . The only exception is the 18.468-nm M1 line within the lowest excited configuration $3p^53d^2$ of the K-like ion. Four of the observed lines, namely, 18.567 nm in the Co-like ion, 17.080 nm and 14.959 nm in the Ca-like ion and 15.962 nm in the K-like ion, are already known from our previous measurements [9]. The other lines in Table I are reported here for the first time. As discussed above, the uncertainty of the measured wavelengths is ± 0.003 nm.

TABLE I: Identified magnetic dipole lines in the experimental spectra between 10 nm and 25 nm. The previously known lines are marked by asterisks. The FAC level numbers within ions are given in square brackets. Other theoretical works: a-[42], b-[26], c-[30], d-[43].

Ion charge	Sequence	λ_{exp} (nm)	λ_{th} (nm)	Lower level	Upper level	A (s ⁻¹)
47	Co	18.567*	18.640, 18.6229 ^a	$3d^9$ [1] $(d_+^5)_{5/2}$	$3d^9$ [2] $(d_-^3)_{3/2}$	2.47(6)
48	Fe	15.511	15.525	$3d^8$ [1] $(d_+^4)_4$	$3d^8$ [6] $((d_-^3)_{3/2}, (d_+^5)_{5/2})_4$	1.01(6)
48	Fe	17.502	17.489	$3d^8$ [2] $(d_+^4)_2$	$3d^8$ [7] $((d_-^3)_{3/2}, (d_+^5)_{5/2})_1$	1.71(6)
48	Fe	18.878	18.956	$3d^8$ [2] $(d_+^4)_2$	$3d^8$ [5] $((d_-^3)_{3/2}, (d_+^5)_{5/2})_2$	1.93(6)
48	Fe	18.988	19.075	$3d^8$ [1] $(d_+^4)_4$	$3d^8$ [4] $((d_-^3)_{3/2}, (d_+^5)_{5/2})_3$	3.22(6)
49	Mn	14.166	14.139	$3d^7$ [1] $(d_+^3)_{9/2}$	$3d^7$ [10] $((d_-^2)_{3/2}, (d_+^4)_2)_{7/2}$	1.76(5)
49	Mn	15.368	15.354	$3d^7$ [1] $(d_+^3)_{9/2}$	$3d^7$ [9] $((d_-^3)_{3/2}, (d_+^4)_4)_{11/2}$	1.89(5)
49	Mn	17.106	17.137	$3d^7$ [1] $(d_+^3)_{9/2}$	$3d^7$ [5] $((d_-^3)_{3/2}, (d_+^4)_2)_{9/2}$	2.23(6)
49	Mn	18.276	18.303	$3d^7$ [3] $(d_+^3)_{5/2}$	$3d^7$ [10] $((d_-^3)_{3/2}, (d_+^4)_2)_{7/2}$	2.72(5)
49	Mn	18.670	18.741	$3d^7$ [2] $(d_+^3)_{3/2}$	$3d^7$ [8] $((d_-^3)_{3/2}, (d_+^4)_2)_{1/2}$	2.56(6)
49	Mn	18.880	18.972	$3d^7$ [1] $(d_+^3)_{9/2}$	$3d^7$ [4] $((d_-^3)_{3/2}, (d_+^4)_2)_{7/2}$	3.57(6)
49	Mn	19.047	19.127	$3d^7$ [2] $(d_+^3)_{3/2}$	$3d^7$ [7] $((d_-^3)_{3/2}, (d_+^4)_4)_{5/2}$	1.03(6)
50	Cr	12.779	12.685	$3d^6$ [1] $(d_+^2)_4$	$3d^6$ [15] $((d_-^3)_{3/2}, (d_+^3)_{5/2})_3$	4.05(5)
50	Cr	13.137	13.105	$3d^6$ [1] $(d_+^2)_4$	$3d^6$ [12] $((d_-^3)_{3/2}, (d_+^3)_{5/2})_4$	3.68(4)
50	Cr	13.886	13.848	$3d^6$ [2] $(d_+^2)_2$	$3d^6$ [15] $((d_-^3)_{3/2}, (d_+^3)_{5/2})_3$	4.92(5)
50	Cr	14.193	14.176	$3d^6$ [2] $(d_+^2)_2$	$3d^6$ [13] $((d_-^3)_{3/2}, (d_+^3)_{5/2})_2$	3.20(5)
50	Cr	15.363	15.363	$3d^6$ [1] $(d_+^2)_4$	$3d^6$ [10] $((d_-^3)_{3/2}, (d_+^3)_{3/2})_3$	1.01(6)
50	Cr	17.133	17.153	$3d^6$ [1] $(d_+^2)_4$	$3d^6$ [8] $((d_-^3)_{3/2}, (d_+^3)_{9/2})_5$	6.57(5)
50	Cr	17.826	17.823	$3d^6$ [3] $(d_+^2)_0$	$3d^6$ [14] $((d_-^3)_{3/2}, (d_+^3)_{5/2})_1$	1.32(6)
50	Cr	19.239	19.317	$3d^6$ [1] $(d_+^2)_4$	$3d^6$ [5] $((d_-^3)_{3/2}, (d_+^3)_{9/2})_4$	3.02(6)
50	Cr	19.684	19.791	$3d^6$ [1] $(d_+^2)_4$	$3d^6$ [4] $((d_-^3)_{3/2}, (d_+^3)_{9/2})_3$	2.56(6)

TABLE I: Identified magnetic dipole lines in the experimental spectra between 10 nm and 25 nm. The previously known lines are marked by asterisks. The FAC level numbers within ions are given in square brackets. Other theoretical works: a-[42], b-[26], c-[30], d-[43].

Ion charge	Sequence	λ_{exp} (nm)	λ_{th} (nm)	Lower level	Upper level	A (s ⁻¹)
51	V	14.531	14.511	$3d^5$ [1] $(d_+)_5/2$	$3d^5$ [9] $((d_-^3)_{3/2}, (d_+^2)_2)_{7/2}$	1.21(5)
51	V	17.215	17.260	$3d^5$ [1] $(d_+)_5/2$	$3d^5$ [5] $((d_-^3)_{3/2}, (d_+^2)_2)_{3/2}$	3.75(6)
51	V	17.660	17.709	$3d^5$ [1] $(d_+)_5/2$	$3d^5$ [3] $((d_-^3)_{3/2}, (d_+^2)_4)_{7/2}$	1.59(6)
51	V	18.996	19.098	$3d^5$ [4] $((d_-^3)_{3/2}, (d_+^2)_4)_{11/2}$	$3d^5$ [13] $((d_-^2)_3, (d_+^3)_{9/2})_{11/2}$	2.31(6)
51	V	21.203	21.370	$3d^5$ [1] $(d_+)_5/2$	$3d^5$ [2] $((d_-^3)_{3/2}, (d_+^2)_4)_{5/2}$	3.40(6)
52	Ti	13.543	13.521	$3d^4$ [5] $((d_-^3)_{3/2}, (d_+)_5/2)_3$	$3d^4$ [17] $((d_-^2)_0, (d_+^2)_4)_4$	1.09(6)
52	Ti	16.890	16.922	$3d^4$ [2] $((d_-^3)_{3/2}, (d_+)_5/2)_1$	$3d^4$ [7] $((d_-^2)_2, (d_+^2)_4)_2$	4.70(6)
52	Ti	17.846	17.905	$3d^4$ [3] $((d_-^3)_{3/2}, (d_+)_5/2)_4$	$3d^4$ [10] $((d_-^2)_2, (d_+^2)_4)_5$	1.65(6)
52	Ti	19.319	19.427, 19.6 ^b	$3d^4$ [1] $(d_+^4)_0$	$3d^4$ [2] $((d_-^3)_{3/2}, (d_+)_5/2)_1$	3.31(6)
52	Ti	19.445	19.568	$3d^4$ [3] $((d_-^3)_{3/2}, (d_+)_5/2)_4$	$3d^4$ [8] $((d_-^2)_2, (d_+^2)_4)_4$	3.02(6)
53	Sc	12.312	12.291	$3d^3$ [1] $(d_-^3)_{3/2}$	$3d^3$ [7] $((d_-^2)_0, (d_+)_5/2)_{5/2}$	2.75(5)
53	Sc	15.785	15.812	$3d^3$ [4] $((d_-^2)_2, (d_+)_5/2)_{9/2}$	$3d^3$ [12] $((d_-)_{3/2}, (d_+^2)_4)_{11/2}$	1.42(6)
53	Sc	16.027	16.056	$3d^3$ [1] $(d_-^3)_{3/2}$	$3d^3$ [6] $((d_-^2)_2, (d_+)_5/2)_{1/2}$	1.02(6)
53	Sc	17.216	17.271	$3d^3$ [1] $(d_-^3)_{3/2}$	$3d^3$ [3] $((d_-^2)_2, (d_+)_5/2)_{3/2}$	2.74(6)
53	Sc	18.867	18.971	$3d^3$ [1] $(d_-^3)_{3/2}$	$3d^3$ [2] $((d_-^2)_2, (d_+)_5/2)_{5/2}$	3.41(6)
54	Ca	14.959*	14.984, 15.010 ^c	$3d^2$ [1] $(d_-^2)_2$	$3d^2$ [4] $((d_-)_{3/2}, (d_+)_5/2)_2$	1.81(6), 1.798(6) ^c
54	Ca	17.080*	17.147, 17.157 ^c	$3d^2$ [1] $(d_-^2)_2$	$3d^2$ [3] $((d_-)_{3/2}, (d_+)_5/2)_3$	3.68(6), 3.683(6) ^c
54	Ca	19.177	19.281, 19.294 ^c	$3d^2$ [2] $(d_-^2)_0$	$3d^2$ [6] $((d_-)_{3/2}, (d_+)_5/2)_1$	1.72(6), 1.771(6) ^c
55	K	15.962*	16.003	$3d$ [1] $(d_-)_{3/2}$	$3d$ [2] $(d_+)_{5/2}$	2.59(6), 1.48(6) ^d
55	K	18.468	18.536	$3p^5 3d^2$ [6] $((p_+^3)_{3/2}, (d_-^2)_2)_{7/2}$	$3p^5 3d^2$ [9] $((p_+^3)_{3/2}, d_-)_{3, d_+} 9/2$	2.99(6)

The atomic levels in Table I are described in jj-coupling, as calculated by the FAC code. The l_{\pm} groups with total zero angular momentum are not shown. For instance, the excited level of the $3d^9$ configuration of the Co-like ion has six $3d_+$ electrons with momentum projections from $m_j = -5/2$ to $m_j = +5/2$ which are omitted in the notation. The numbers in square brackets in the level notation columns show the calculated level number within the corresponding ion (the ground level is number 1 and so on).

There are several lines from neighboring ions that have very close wavelengths, e.g., 18.878 nm in Fe-like and 18.880 nm in Mn-like ion, or 15.368 nm in Mn-like and 15.363 nm in Cr-like ion. For such cases the wavelengths were determined from a spectrum where one of the lines was strong while the other was weak due to the shifted ionization distribution.

The wavelengths for other lines were obtained by averaging over several measured spectra.

Table I also shows our calculated wavelengths and transition probabilities as well as several other theoretical results [26, 30, 42, 43]. In most cases the present results agree quite well with the measured wavelengths although for several lines the difference is rather large, as much as 0.5 %. This probably reflects difficulties in atomic structure calculations for such complex ions. Most of the calculated transition probabilities are between 10^5 s^{-1} and $5 \cdot 10^6 \text{ s}^{-1}$. The only line with a smaller probability of $A = 3.68 \cdot 10^4 \text{ s}^{-1}$ is the 13.137 nm J=4–J=4 transition in Cr-like W. Note also that the recent RMBPT calculations for Ca-like W [30] agree with our transition probabilities to within a few percent.

The energy structure of the $3d^n$ ions and population flux analysis explain why only the forbidden M1 lines are visible between 10 nm ($\Delta E \approx 124 \text{ eV}$) and 25 nm ($\Delta E \approx 50 \text{ eV}$) under EBIT conditions. Normally, the strongest E1 lines in a collisionally-dominated spectrum are due to transitions between the ground configuration and lowest excited configuration of opposite parity. There is, however, a relatively large energy gap between $3p^6 3d^n$ and $3p^5 3d^{n+1}$. Our calculations with FAC show that the $3p - 3d$ excitation energy in tungsten ions is about (300–400) eV. Figure 4 shows the calculated energy levels below 500 eV for Co-like through K-like ions of W. The levels of the ground configuration are represented by horizontal lines, and the vertical bars show the spread of the $3p^5 3d^{n+1}$ configuration. For W^{47+} , W^{48+} , W^{49+} , and W^{55+} , the energy gap between these configurations is larger than 124 eV, so that the corresponding E1 lines have wavelengths smaller than 10 nm. For the remaining ions, the highest $3d^n$ levels are rather close to the lower edge of $3p^5 3d^{n+1}$ manifold. However, only a few possible EUV transitions obey the $|\Delta J| \leq 1$ selection rule for E1 lines and moreover, those transitions are greatly suppressed by small branching ratios due to stronger soft x-ray decays into the lowest levels of the ground configuration.

Some transitions between higher- n states, for instance, $n=4-5$ transitions in Fe-like and Mn-like ions, also fall into the 10–25 nm range. In low-density plasmas, the populations of the lowest excited levels of $3d^n$ are much higher than those of the high-excited states and therefore only M1 lines are strong. When the density is high, the populations approach the Boltzmann values which are of the same order for all levels in an ion. Since E1 rates between the higher states are much stronger than the M1 probabilities, only the E1 lines will be present at high densities.

As mentioned above, four of the spectral lines in table I have already been observed in

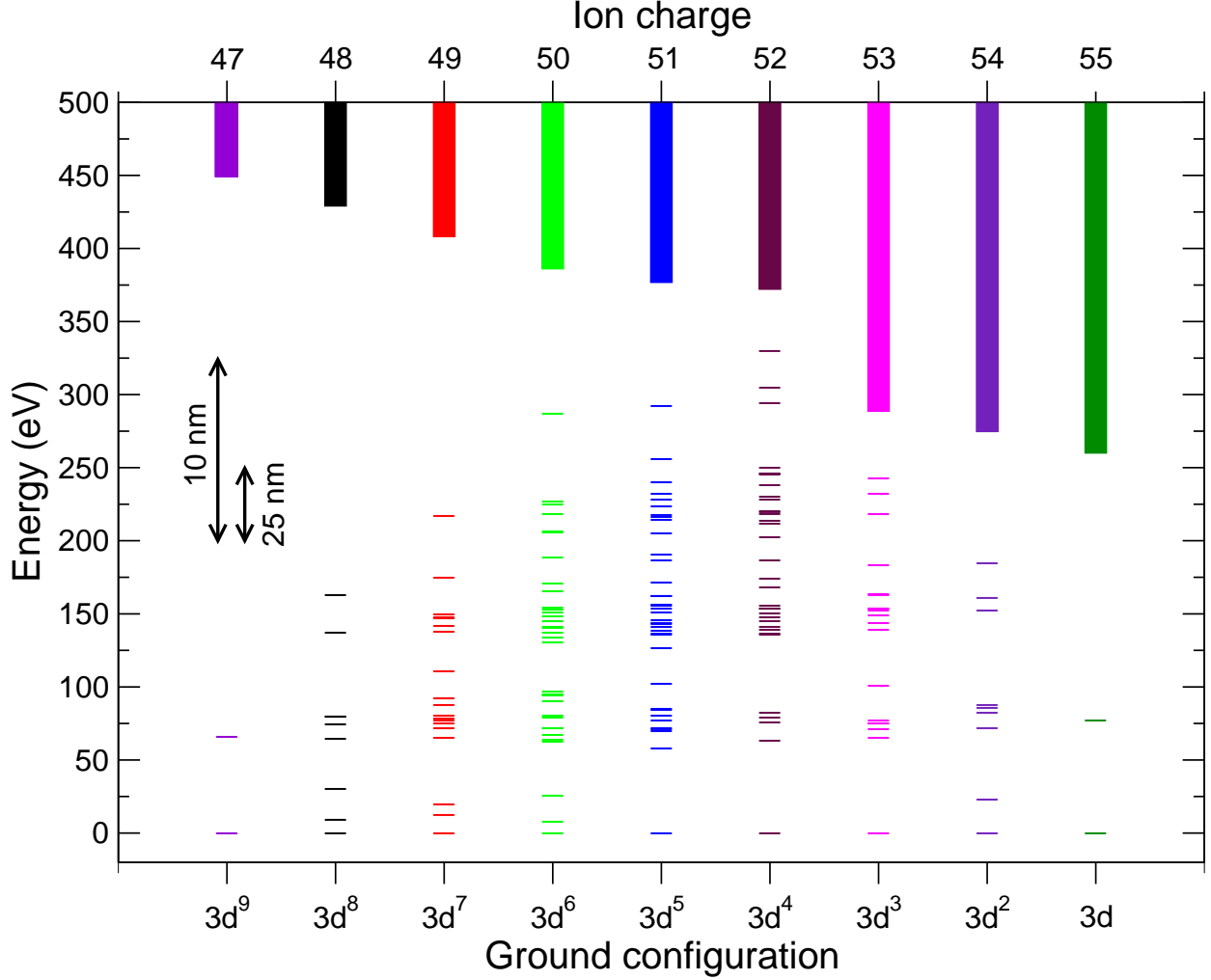


FIG. 4. Calculated energy levels of the $3p^6 3d^n$ configurations in W^{47+} through W^{55+} . The vertical bars at the top show the spread of the $3p^5 3d^{n+1}$ configurations below 500 eV.

our previous experiments. While the new wavelengths for the lines from Ca- and K-like ions agree with the known values within experimental uncertainties, the 18.567 ± 0.003 nm wavelength for the M1 transition in Co-like ion is shifted with respect to our previous value of 18.578 ± 0.002 nm [10]. To address this problem, we reexamined the 4228 eV spectrum of Ref. [10] where this line was identified for the first time. As was pointed out in the original publication, the line was strongly blended by third-order lines; our current analysis shows that its wavelength should therefore have been assigned a larger uncertainty. For the lowest beam energies of the present experiment, the M1 line in the Co-like ion is the strongest in the spectrum (Fig. 1) so that its wavelength was determined very reliably. Therefore, the presently measured wavelength of 18.567 ± 0.003 nm replaces the previous value of Ref. [10].

Our new wavelength agrees better with the semi-empirical wavelength of 18.541 ± 0.032 nm [44].

V. DIAGNOSTICS WITH THE M1 LINES

The diagnostic potential of the M1 lines is based on several features. First, the intensity ratios for lines from different ions can conveniently serve as a diagnostics of temperature and ionization balance. It is also helpful that the spectral window for these lines is rather narrow, which reduces dependence of spectrometer efficiency on wavelength. Finally, and most importantly, these forbidden lines can be used to diagnose electron density in fusion plasmas.

Various methods have been developed for spectroscopic diagnostics of electron density [45]. Such techniques make use, for instance, of line intensity ratios or collisional widths of isolated lines. The line ratio diagnostics is normally based on comparison of allowed and forbidden lines which are populated by similar mechanisms (normally, by excitation from the ground state) and whose radiative decay rates differ by orders of magnitude. For low densities, when collisional depopulation rates are much smaller than either of the radiative rates, the intensities of both allowed and forbidden lines vary linearly with density and therefore their ratio is independent of n_e . When collisional rates become comparable with the probabilities of forbidden transitions, the ratio shows sensitivity to n_e , typically over one or two orders in n_e . A well-known example is the resonance-to-intercombination-line ratio in He-like ions which has been widely used in plasma diagnostics [46].

While the measured low-density spectra from the $3d^n$ ions of tungsten contain no strong E1 lines, the decay rates for the observed M1 lines vary by as much as two orders of magnitude, and hence one may expect at least some sensitivity of line ratios to density variations. In order to analyze the n_e -dependence of the M1 line intensities under typical conditions of hot fusion plasmas, we performed another set of calculations with NOMAD using a Maxwellian electron energy distribution function and including dielectronic recombination within the Burgess-Merts-Cowan-Magee approximation [47]. The steady-state solutions of the rate equations were determined for electron densities in the range of $n_e = 10^{10} - 10^{17}$ cm⁻³ at electron temperatures $T_e^z \approx I_z$ where I_z is the ionization potential of the ion under study. It was recently shown [48] that unlike the low- Z elements, the typical temperatures

of the maximal abundance for highly-charged W ions are on the order or even larger than the corresponding ionization potentials, and therefore the condition $T_e^z \approx I_z$ is well justified for hot steady-state plasmas. Also, since the excitation energies of the levels within ground configurations are much smaller than T_e^z , the intensity ratios for the EUV lines would only be marginally sensitive to electron temperature. Finally, since the intensity ratios involve only lines from the same ionization stage, the conclusions will not depend on ionization distribution.

We have already mentioned above that the collisional depopulation of the upper level is the primary physical process resulting in density sensitivity of a spectral line. The effect of collisions on level population can be approximately parameterized by their fraction in the total depopulation rate (see also [46]):

$$\alpha_i(n_e) = \frac{\sum_j n_e R_{ij}^{col}}{\sum_{j<i} A_{ij}^{rad} + \sum_j n_e R_{ij}^{col}} \quad (4)$$

where $\sum n_e R_{ij}^{col}$ includes all collisional processes depopulating level i , such as excitation, deexcitation and ionization. The low-density coronal limit corresponds to $\alpha_i \rightarrow 0$, and in the high-density Boltzmann (LTE) limit $\alpha_i \rightarrow 1$. The transitional region for an atomic state can be defined by the condition

$$0.1 < \alpha_i(n_e) < 0.9, \quad (5)$$

which covers about two orders of magnitude in n_e , as follows from Eq. (4). This region of n_e determines the range of densities for a spectral line that are most promising for diagnostics when compared with other lines that are still in a coronal limit. Figure 5 shows the calculated transitional regions of n_e for the upper levels listed in table I including, for completeness, the levels of Co-like $3d^9$ and K-like $3d$ ions. It follows from this plot that, for instance, level 9 in the Mn-like ion, from which the 15.368 nm line originates, decays only radiatively ($\alpha < 0.1$) at densities smaller than $2 \cdot 10^{13} \text{ cm}^{-3}$, while electron collisions are the dominant depletion mechanism for this level above $1.5 \cdot 10^{15} \text{ cm}^{-3}$. One can see that for almost every ion there exist levels with rather different ranges of α_i variations, and therefore one may expect to find several pairs of lines whose intensity ratio may be used for density diagnostics. Moreover, the transitional regions for a large number of levels overlap with the typical range of n_e in core fusion plasmas (marked by the vertical dashed lines).

The best n_e -sensitive line intensity ratios for ions of tungsten from W^{48+} to W^{53+} are presented in Fig. 6 and are discussed below. The line intensities were defined as $I = N \cdot A \cdot \Delta E$

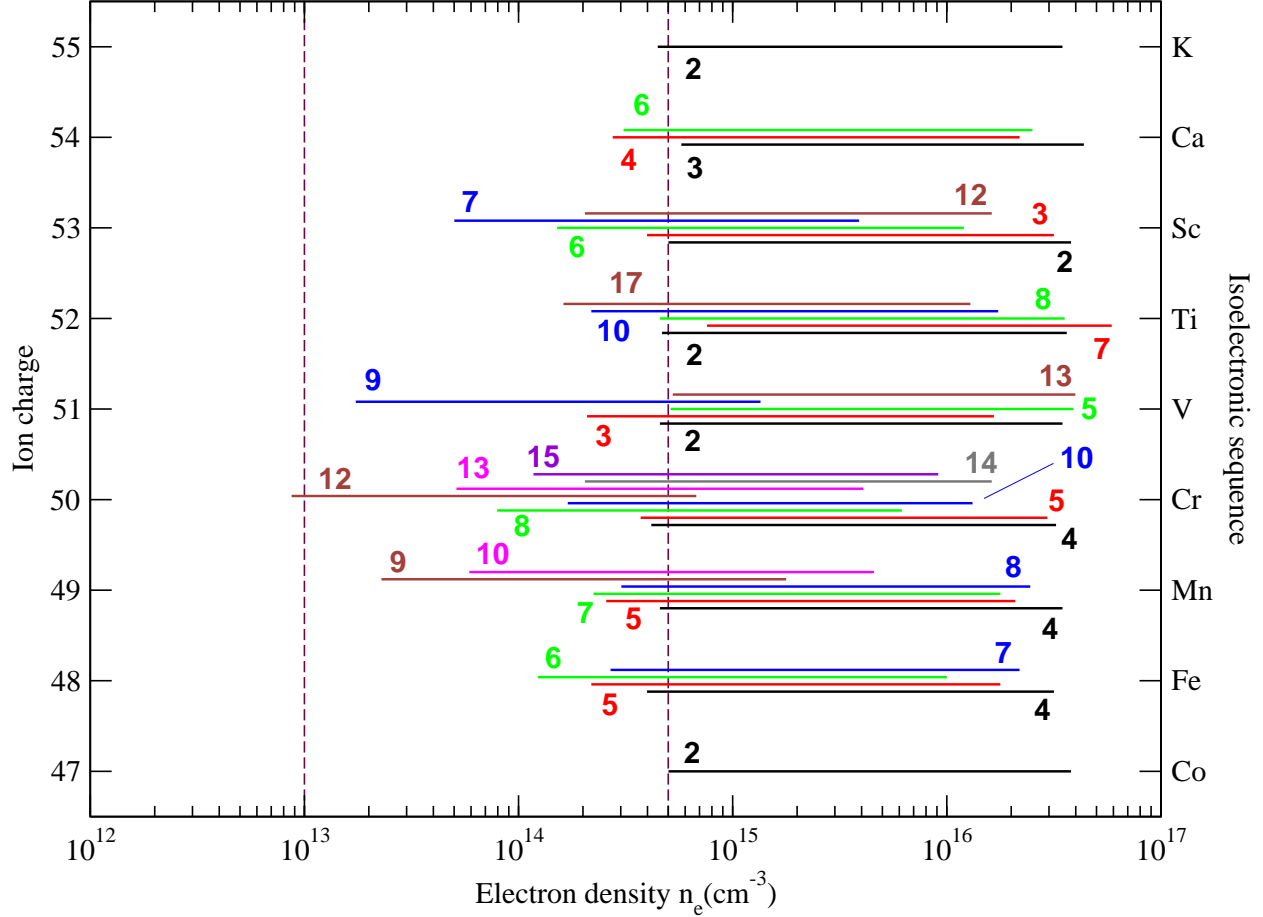


FIG. 5. Transitional ($0.1 < \alpha_i < 0.9$) regions of densities for the upper levels of M1 lines from table I. The numbers are the calculated level numbers in a corresponding ion. The range of typical electron densities of core fusion plasmas is shown by vertical dashed lines.

where N is the upper level population (in cm^{-3}), A is the transition probability (in s^{-1}), and ΔE is the photon energy (in J).

A. Fe-like W^{48+}

Among the four identified lines in the Fe-like ion, the ratio of lines originating from levels 4 and 6 offers the best sensitivity to density variations. However, the transitional regions of n_e for these levels, as follows from Fig. 5, are not too different and therefore the line ratio would not change significantly. Indeed, as shown in the top left panel of Fig. 6, the intensity ratio for the spectral lines at 18.988 nm and 15.511 nm varies only within a factor of 2.3 between $3 \cdot 10^{14} \text{ cm}^{-3}$ and 10^{16} cm^{-3} . Another complication arises from the overlap between

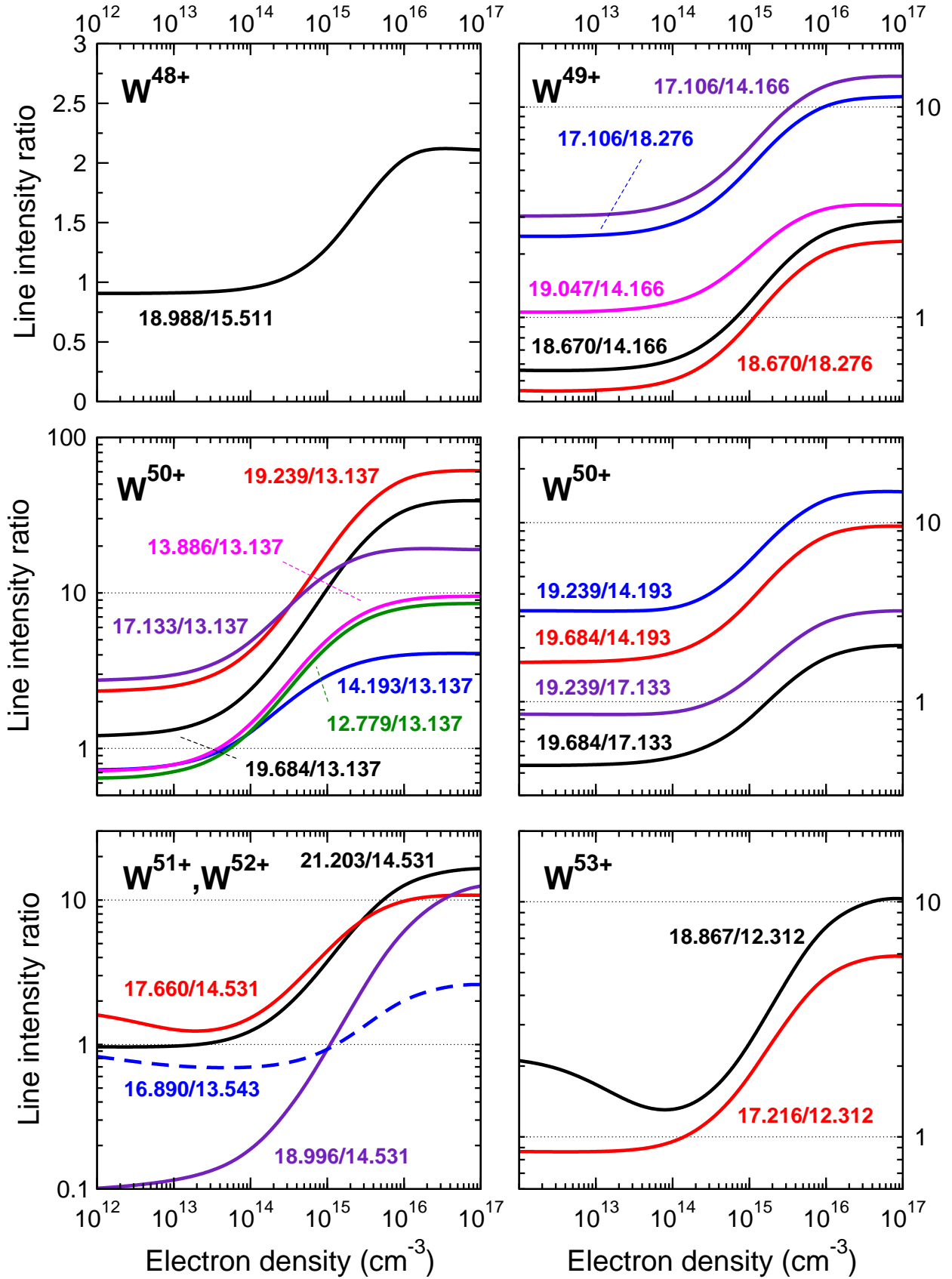


FIG. 6. Density-sensitive line ratios for ions of tungsten from W^{48+} to W^{53+} .

the 18.988 nm lines and the 19.047 nm line in the next Mn-like ion W^{49+} .

B. Mn-like W^{49+}

Although the seven identified transitions in Mn-like W^{49+} offer several pairs of lines of potential usage in density diagnostics (top right panel in Fig. 6), it would be rather challenging for experimentalists to reliably isolate most of these lines from the other lines that originate from the neighboring ions. It seems that the 18.670/18.276 ratio that increases by a factor of 5 between 10^{14} cm^{-3} and 10^{16} cm^{-3} may actually be the best choice since these two lines are well isolated in the measured spectrum.

C. Cr-like W^{50+}

Among all $3d^n$ ions of tungsten, the Cr-like ion offers the largest number of n_e -sensitive line pairs. This is due to both the largest number of identified lines and the most separated regions of density sensitivity for different lines. The population of level 12, which is responsible for the strong and well isolated line at 13.137 nm, starts to deviate from coronal behavior at electron densities as low as $9 \cdot 10^{12} \text{ cm}^{-3}$ (Fig. 5). The strongest radiative transition from this level has probability of only $3.68 \cdot 10^4 \text{ s}^{-1}$ as compared with the typical M1 probabilities of 10^5 s^{-1} and larger (Table I) and therefore this level becomes collisionally depleted at lower electron densities. The line ratios involving the 13.137 nm line, presented in the middle left panel of Fig. 6, show the strongest dependence on n_e : for instance, the 19.684/13.137 ratio of two strong and isolated lines varies by a factor of 30 between 10^{12} cm^{-3} and 10^{16} cm^{-3} . The ratios with other lines (middle right panel) vary within smaller limits, from 3 to 6.

D. V-like W^{51+}

The transitional regions for the levels of the V-like ion are mostly between $2 \cdot 10^{14} \text{ cm}^{-3}$ and $2 \cdot 10^{16} \text{ cm}^{-3}$. However, electron collisions start to depopulate level 9 at much lower densities of about $2 \cdot 10^{13} \text{ cm}^{-3}$ and thus the line ratios involving a strong isolated line at 14.531 nm can be very sensitive to electron density. For instance, the ratio 18.996/14.531 varies by two orders of magnitude, between 0.1 and 10, for the electron density range of

$(10^{13}\text{--}10^{17})\text{ cm}^{-3}$.

E. Ti-like W^{52+}

Figure 5 shows that the transitional regions of n_e for the $3d^4$ levels in Ti-like ion are very close, and therefore the intensity ratios for the observed M1 lines do not exhibit significant n_e -dependence. We only present a single line ratio 16.890/13.543 (dashed line in the bottom left panel of Fig. 6) which only changes within a factor of 3 within the discussed range of n_e .

F. Sc-like W^{53+}

The two line ratios for the Sc-like ion, 18.867/12.312 and 17.216/12.312, show significant variation between 10^{14} cm^{-3} and 10^{16} cm^{-3} . The former ratio is not monotonic, as is seen from Fig. 6: the low-density limit of about 2 drops to approximately 1.3 before climbing to the value of 10 at the high-density limit. This dip results from the presence of other metastable levels of $3d^3$ that interact with the upper levels of those lines.

VI. CONCLUSIONS

In this paper we presented measurements and identifications of forbidden magnetic-dipole lines within ground configurations of all $3d^n$ ions of tungsten, from Co-like W^{47+} to K-like W^{55+} . Two sets of EUV spectra between 10 nm and 20 nm, independently measured two years apart, excellently agreed with each other, thereby confirming a very good reproducibility of the results. A total of 37 new spectral lines were identified in the spectra.

The identification of the observed M1 lines was based on extensive collisional-radiative modeling of spectra from non-Maxwellian plasma of EBIT. We introduced a new scheme for level grouping in order to reduce the total number of states in our CR model to a tractable level. The calculated spectra agree very well with the measured ones, thereby providing unambiguous determination of line identifications.

The importance of the measured magnetic-dipole lines for spectroscopic diagnostics of hot plasmas stems from several factors. First, the lines are located within a rather narrow range

of wavelengths, which facilitates their measurements and reduces dependence on variation of spectrometer efficiency with wavelength. Second, most of the lines are well isolated with only a few overlapping to some degree. Third, the intensity ratios of spectral lines from different ions can be used to infer electron temperature and ionization balance over a large range of plasma density. Finally, as was shown here with a detailed collisional-radiative modeling of Maxwellian plasmas, a large number of line intensity ratios are sensitive to electron density in the range of magnetic fusion devices. All these features make the M1 lines in $3d^n$ ions of tungsten especially useful for plasma diagnostics.

ACKNOWLEDGMENTS

We thank J.M. Pomeroy, J.N. Tan, and S.M. Brewer for assistance during the first experimental phase of this work. This work is supported in part by the Office of Fusion Energy Sciences of the U.S. Department of Energy and by the Research Associate Program of the National Research Council.

-
- [1] R. J. Hawryluk, D. Campbell, G. Janeschitz, P. Thomas, R. Albanese, R. Ambrosino, C. Bachmann, L. Baylor, M. Becoulet, I. Benfatto, J. Bialek, A. Boozer, A. Brooks, R. Budny, T. Casper, M. Cavinato, J.-J. Cordier, V. Chuyanov, E. Doyle, T. Evans, G. Federici, M. Fenstermacher, H. Fujieda, K. G'al, A. Garofalo, L. Garzotti, D. Gates, Y. Gribov, P. Heitzenroeder, T. Hender, N. Holtkamp, D. Humphreys, I. Hutchinson, K. Ioki, J. Johner, G. Johnson, Y. Kamada, A. Kavin, C. Kessel, R. Khayrutdinov, G. Kramer, A. Kukushkin, K. Lackner, I. Landman, P. Lang, Y. Liang, J. Linke, B. Lipschultz, A. Loarte, G. Loesser, C. Lowry, T. Luce, V. Lukash, S. Maruyama, M. Mattei, J. Menard, M. Merola, A. Mineev, N. Mitchell, E. Nardon, R. Nazikian, B. Nelson, C. Neumeyer, J.-K. Park, R. Pearce, R. Pitts, A. Polevoi, A. Portone, M. Okabayashi, P. Rebut, V. Riccardo, J. Roth, S. Sabbagh, G. Saibene, G. Sannazzaro, M. Schaffer, M. Shimada, A. Sen, A. Sips, C. Skinner, P. Snyder, R. Stambaugh, E. Strait, M. Sugihara, E. Tsitrone, J. Urano, M. Valovic, M. Wade, J. Wesley, R. White, D. Whyte, S. Wu, M. Wykes, and L. Zakharov, *Nucl. Fusion* **49**, 065012 (2009).
- [2] S. B. Utter, P. Beiersdorfer, and G. V. Brown, *Phys. Rev. A* **61**, 030503 (2000).

- [3] J. V. Porto, I. Kink, and J. D. Gillaspay, *Phys. Rev. A* **61**, 054501 (2000).
- [4] S. B. Utter, P. Beiersdorfer, and E. Träbert, *Can. J. Phys.* **80**, 1503 (2002).
- [5] P. Neill, C. Harris, A. S. Safronova, S. Hamasha, S. Hansen, U. I. Safronova, and P. Beiersdorfer, *Can. J. Phys.* **82**, 931 (2004).
- [6] C. Biedermann, R. Radtke, J.-L. Schwob, P. Mandelbaum, R. Doron, T. Fuchs, and G. Fußmann, *Phys. Scr.* **T92**, 85 (2001).
- [7] Yu. Ralchenko, J. N. Tan, J. D. Gillaspay, J. M. Pomeroy, and E. Silver, *Phys. Rev. A* **74**, 042514 (2006).
- [8] Yu. Ralchenko, J. Reader, J. M. Pomeroy, J. N. Tan, and J. D. Gillaspay, *J. Phys. B* **40**, 3861 (2007).
- [9] Yu. Ralchenko, I. N. Draganic, J. N. Tan, J. D. Gillaspay, J. M. Pomeroy, J. Reader, U. Feldman, and G. E. Holland, *J. Phys. B* **41**, 021003 (2008).
- [10] Yu. Ralchenko, J. Reader, J. M. Pomeroy, J. N. Tan, and J. D. Gillaspay, *J. Phys. B* **40**, 3861 (2007).
- [11] J. D. Gillaspay, I. N. Draganić, Y. Ralchenko, J. Reader, J. N. Tan, J. M. Pomeroy, and S. M. Brewer, *Phys. Rev. A* **80**, 010501 (2009).
- [12] J. Clementson, P. Beiersdorfer, and M. F. Gu, *Phys. Rev. A* **81**, 012505 (2010).
- [13] Y. Podpaly, J. Clementson, P. Beiersdorfer, J. Williamson, G. V. Brown, and M. F. Gu, *Phys. Rev. A* **80**, 052504 (2009).
- [14] T. Pütterich, R. Neu, C. Biedermann, R. Radtke, and ASDEX Upgrade Team, *J. Phys. B* **38**, 3071 (2005).
- [15] T. Pütterich, R. Neu, R. Dux, A. D. Whiteford, M. G. O’Mullane, and ASDEX Upgrade Team, *Plasma Phys. Contr. Fusion* **50**, 085016 (2008).
- [16] J. Yanagibayashi, T. Nakano, A. Iwamae, H. Kubo, M. Hasuo, and K. Itami, *J. Phys. B* **43**, 144013 (2010).
- [17] C. S. Harte, C. Suzuki, T. Kato, H. A. Sakaue, D. Kato, K. Sato, N. Tamura, S. Sudo, R. D’Arcy, E. Sokell, J. White, and G. O’Sullivan, *J. Phys. B* **43**, 205004 (2010).
- [18] A. E. Kramida and T. Shirai, *J. Phys. Chem. Ref. Data* **35**, 423 (2006).
- [19] A. E. Kramida and T. Shirai, *At. Data Nucl. Data Tables* **95**, 305 (2009).
- [20] Yu. Ralchenko, A. E. Kramida, J. Reader, and NIST ASD Team, “NIST Atomic Spectra Database, v.4.0.1,” (2010), <http://physics.nist.gov/asd>.

- [21] R. Neu, K. B. Fournier, D. Bolshukhin, and R. Dux, *Phys. Scr.* **T92**, 307 (2001).
- [22] N. Tragin, J.-P. Geindre, P. Monier, J.-C. Gauthier, C. Chenais-Popovics, J.-F. Wyart, and C. Bauche-Arnoult, *Phys. Scr.* **37**, 72 (1988).
- [23] R. Neu, K. B. Fournier, D. Schlögl, and J. Rice, *J. Phys. B* **30**, 5057 (1997).
- [24] R. Radtke, C. Biedermann, G. Fussmann, J. L. Schwob, P. Mandelbaum, and R. Doron, in *Atomic and Plasma-Material Interaction Data for Fusion, Vol. 13*, edited by R. E. H. Clark (International Atomic Energy Agency, Vienna, 2007) p. 45.
- [25] U. Feldman, P. Indelicato, and J. Sugar, *J. Opt. Soc. Am. B* **8**, 3 (1991).
- [26] U. Feldman, R. Doron, M. Klapisch, and A. Bar-Shalom, *Phys. Scr.* **63**, 284 (2001).
- [27] R. Doron and U. Feldman, *Phys. Scr.* **64**, 319 (2001).
- [28] V. Jonauskas, R. Kisielius, A. Kynienė, S. Kučas, and P. H. Norrington, *Phys. Rev. A* **81**, 012506 (2010).
- [29] P. Quinet, V. Vinogradoff, P. Palmeri, and E. Biémont, *J. Phys. B* **43**, 144003 (2010).
- [30] U. I. Safronova and A. S. Safronova, *J. Phys. B* **43**, 074026 (2010).
- [31] “NIST Atomic Spectra Bibliographic Databases,” (2010), <http://physics.nist.gov/asbib>.
- [32] Yu. Ralchenko, *J. Phys. B* **40**, F175 (2007).
- [33] J. D. Gillaspy, *Phys. Scr.* **T71**, 99 (1997).
- [34] B. Blagojevic, E. O. L. Bigot, K. Fahy, A. Aguilar, K. Makonyi, E. Takacs, J. N. Tan, J. M. Pomeroy, J. H. Burnett, J. D. Gillaspy, and J. R. Roberts, *Rev. Sci. Instrum.* **76**, 083102 (2005).
- [35] K. Fahy, E. Sokell, G. O’Sullivan, A. Aguilar, J. M. Pomeroy, J. N. Tan, and J. D. Gillaspy, *Phys. Rev. A* **75**, 032520 (2007).
- [36] G. E. Holland, C. N. Boyer, J. F. Seely, J. N. Tan, J. M. Pomeroy, and J. D. Gillaspy, *Rev. Sci. Instrum.* **76**, 073304 (2005).
- [37] Yu. Ralchenko and Y. Maron, *J. Quant. Spectr. Rad. Transfer* **71**, 609 (2001).
- [38] S. Otranto, R. E. Olson, and P. Beiersdorfer, *Phys. Rev. A* **73**, 022723 (2006).
- [39] M. F. Gu, *Can. J. Phys* **86**, 675 (2007).
- [40] S. B. Hansen, J. Bauche, C. Bauche-Arnoult, and M. F. Gu, *High En. Dens. Phys.* **3**, 109 (2007).
- [41] I. N. Draganić, Y. Ralchenko, J. Reader, J. D. Gillaspy, J. N. Tan, J. M. Pomeroy, S. M. Brewer, and D. Osin, *J. Phys. B* **44**, 025001 (2011).

- [42] K. B. Fournier, *At. Data Nucl. Data Tables* **68**, 1 (1998).
- [43] E. Charro, Z. Curiel, and I. Martín, *Astron. Astrophys.* **387**, 1146 (2002).
- [44] J. O. Ekberg, U. Feldman, J. F. Seely, C. M. Brown, J. Reader, and N. Acquista, *J. Opt. Soc. Am. B* **4**, 1913 (1987).
- [45] H. R. Griem, *Principles of Plasma Spectroscopy* (Cambridge University Press, 1997).
- [46] H.-J. Kunze, *Introduction to plasma spectroscopy* (Springer-Verlag, 2009).
- [47] R. D. Cowan, *The theory of atomic structure and spectra* (University of California Press, 1981).
- [48] Yu. Ralchenko, J. J. Abdallah, A. Bar-Shalom, J. Bauche, C. Bauche-Arnoult, C. Bowen, H.-K. Chung, J. Colgan, G. Faussurier, C. J. Fontes, M. Foster, F. de Gaufridy de Dortan, I. Golovkin, S. B. Hansen, R. W. Lee, V. Novikov, J. Oreg, O. Peyrusse, M. Poirier, A. Sasaki, H. Scott, and H. L. Zhang, in *ATOMIC PROCESSES IN PLASMAS: Proceedings of the 16th International Conference on Atomic Processes in Plasmas*, Vol. 1161 (2009) p. 242.